ELSEVIER

Journal of Electroanalytical Chemistry 538–539 (2002) 13–23

Journal of Electroanalytical Chemistry

www.elsevier.com/locate/jelechem

Simultaneous measurements of conductivity and thickness for polymer electrolyte films: a simulation study

A.D. Fitt [a], J.R. Owen [b,*]

[a] Faculty of Mathematical Studies, University of Southampton, Southampton SO17 1BJ, UK
[b] Electrochemistry Group, Department of Chemistry, University of Southampton, Southampton SO17 1BJ, UK

Received 10 May 2002; received in revised form 4 July 2002; accepted 18 July 2002

Abstract

Planar cells provide an attractive alternative to traditional cylindrical cells for polymer electrolyte conductivity measurement as they not only allow sample quantity minimisation but also equilibration with vapour. They are also a key component in the parallel screening of combinatorially synthesised arrays of samples. A finite element simulation technique is used to calculate the complex cell constants of planar cells for a wide range of cell geometries. The real part and the phase of the cell impedance at the high frequency limit are identified as the most sensitive indicators of the polymer thickness, and thereby the cell constant, through which the measured impedance value yields the conductivity. Cell geometries are identified for which the conductivity may be determined in an optimally accurate fashion.

Keywords: Polymer electrolyte; Impedance; Finite element analysis; Combinatorial screening; Planar cells; Microband electrodes; Complex cell constant

1. Introduction

Polymer electrolytes belong to an important class of electrochemical materials with applications in solid-state electrochemical devices such as thin film batteries [1], fuel cells [2], electrochromic displays [3] and chemical sensors. Many new materials are currently being synthesised in efforts to discover compositions that exhibit improved properties, in particular the ionic conductivity for lithium ions or protons. In many cases it is also important to measure changes in the conductivity due to the uptake of water, non-aqueous solvents, or other substances that may be absorbed from the ambient atmosphere.

Normally conductivity measurements are performed in a cylindrical cell [4] of the type shown in Fig. 1. An alternating potential is used to bypass the ion-blocking interfaces between the sample and inert, electronically conducting contacts [5]. The complex impedance, Z (Ω) of the cell is measured as a function of frequency f (Hz), and the results can be analysed to give a single value of the polymer resistance, R (Ω), using the equivalent circuit of Fig. 2. The extraction of a single, real, resistance from the frequency-dependent complex impedance data relies on linear extrapolations of impedance data to the real axis either from the line due to the series RC_{dl} combination at low frequency (where C_{dl} (F) is the double layer capacitance), or the semicircular arc due to the parallel RC_g combination (where C_g is the dielectric capacitance) at high frequency (see Fig. 2). It should be noted that the validity of these extrapolations depends on the one-dimensional nature of the apparatus, which causes the potential and current density to be constant perpendicular to the cylinder axis. The conductivity σ (S m^{-1}) is then obtained from the measured resistance using Eq. (1).

$$\sigma = k/R = \ell/(AR) \tag{1}$$

where ℓ is the sample thickness (m), A is the sample cross-sectional area (m^2) and the cell constant k is given simply by ℓ/A (m^{-1}).

* Corresponding author. Tel.: +44-1703-592-184; fax: +44-1703-676-960.
E-mail address: jro@soton.ac.uk (J.R. Owen).

0022-0728/02/$ - see front matter
PII: S0022-0728(02)01174-9

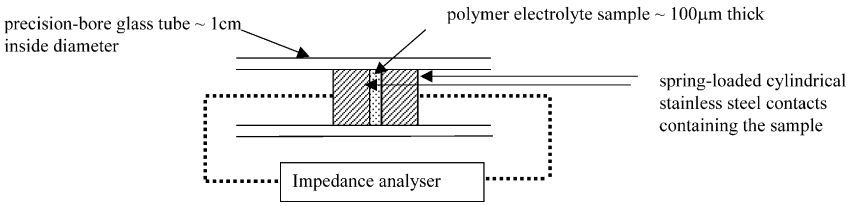

Fig. 1. Conventional cylindrical cell design for ionic conductivity measurements on polymer electrolytes.

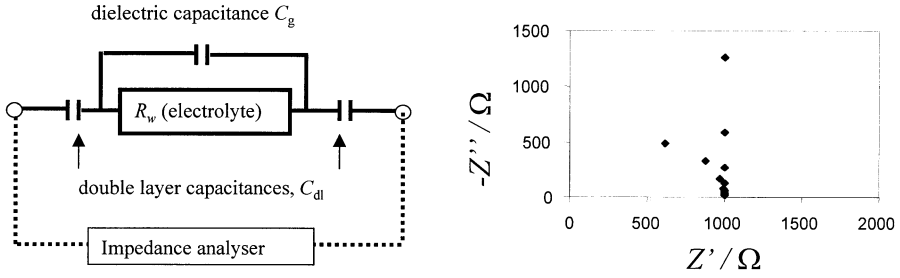

Fig. 2. Equivalent circuit corresponding to the cell of Fig. 1 and an illustrative simulated complex impedance (Nyquist) plot for $R_w = 1000\ \Omega$, $C_{dl} = 5 \times 10^{-6}$ F, $C_g = 5 \times 10^{-10}$ F, $f_{max} = 10^7$ Hz, $f_{min} = 10^3$ Hz.

Although such cells give a straightforward relationship between the impedance and the conductivity, their disadvantages are that a rather large sample size is required and, more importantly, the difficulty of equilibration with an ambient vapour such as water or a solvent. Fig. 3 illustrates an alternative cell [6] for measuring the conductivity of a polymer electrolyte in which the quantity of sample is minimised. The polymer is applied as a thin film mainly over the unmasked area, covering the electrodes and the gap between them. This configuration allows fast equilibration with the vapour phase, so that the composition can be changed (e.g. by humidification) during the course of successive conductance measurements. The dimensions suggested in Fig. 3 have been designed to give easily measured resistances for samples with conductivities in the range 10^1 S m$^{-1} > \sigma > 10^{-4}$ S m^{-1}. The appropriate frequency range of the simulations was determined as follows. Although an upper frequency limit of 10 MHz was chosen to correspond to the maximum frequency of most impedance analysers, it was found that the most interesting impedance phenomena occurred at lower frequencies as shown in the figures. The low frequency limit was 100 Hz, which was well below the minimum value of the quantity ($1/RC$) for a sample of conductivity 10^1 S m^{-1} and an interfacial capacitance of 0.1 F m^{-2} for the cell dimensions under consideration.

A sample volume of about one-tenth of that required for a cylindrical cell is particularly advantageous for the application of combinatorial synthesis techniques. A disadvantage of this method is that the cell constant is more difficult to calculate, and even the procedure for extrapolating the impedance to give the resistance is not straightforward. Although changes in conductivity with temperature and ambient gas are easily monitored,

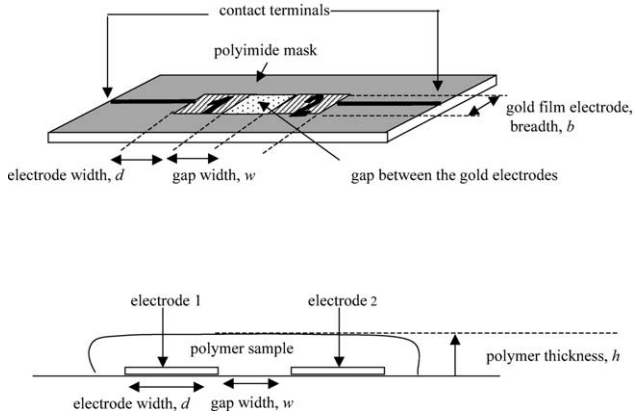

Fig. 3. The proposed planar cell for conductivity measurement. Typically, $d \sim 200$ μm, $w \sim 20$–200 μm, $h \sim 10$–200 μm, $b \sim 500$ μm.

absolute values are subject to errors in the determination of the cell constant.

In our previous work [6] on planar cells, values of the cell constant were calculated using a Schwartz–Christoffel (SC) transformation method, which yielded an analytical solution to the case with semi-infinite, non-blocking electrodes. This suggested an experimental procedure in which a combination of resistance measurements for two cells with different gap widths could yield both the conductivity and the film thickness. However, in that work the blocking nature of the interface was ignored in the derivation of the cell constant on the grounds that, in the high frequency limit, the impedance of the double layer capacitance tends to zero. Although this approximate treatment gave absolute conductivity values accurate to 5%, subsequent work has shown that the omission of the interfacial capacitive impedance cannot be justified over

a wide variety of planar cell geometries and polymer conductivities. Furthermore, a subsequent analysis showed that the simple equivalent circuit of Fig. 2 cannot now be applied since the cell geometry is no longer essentially one-dimensional.

The current work recognises the fact that to effect a proper description of the general behaviour of a planar cell over a range of frequencies requires the introduction of a complex cell constant that takes into account the phase variations of the impedance. The complex cell constant, K, (m^{-1}) may be defined by Eq. (2) and is a function of the four variables b, d, h and w defined in Fig. 3 as well as the frequency, f.

$$K = \sigma Z \ (b, d, h, w; f) \tag{2}$$

The overall objective of the current work is therefore to understand the relationship between the complex cell constant and the cell parameters in order to specify a viable experimental procedure and method of interpretation of results that will yield reliable conductivity values for films of unknown thickness.

Since the SC approach cannot easily be generalised to cover the effects of interfacial capacitance and the finite geometry boundary conditions, in this work we have used a finite element simulation approach, which is described briefly below. Further details will be given in a manuscript currently under preparation by the present authors. Work on the experimental application of the technique is also in progress and involves the fabrication of multiple electrode arrays using photolithographical techniques for combinatorial electrolyte deposition. This work will be reported separately.

2. A preliminary analysis

The geometry of Fig. 3 may be simplified to two dimensions by assuming that the electrode breadth, b, is large compared to d and w, and ignoring end effects. In this two-dimensional model, the product of the resistance and cell breadth Rb is represented by $\bar{R}$ (Ω m) and the cell constant $\bar{K}$ ($= Kb$) is dimensionless. Also the interfacial capacitance per unit breadth, C_{dl}/b will be designated by $\bar{C}_{dl}$ (F m^{-1}) and the two-dimensional conductivity σb by $\bar{\sigma}$ (S). Henceforth all 'two-dimensional' quantities will be distinguished by an overbar.

A further simplification will be to assume that the admittance due to the dielectric permittivity is negligible over the frequency range of measurement. The high frequency limit of the impedance will thus be represented by a single, real value and the only frequency dispersion under consideration will be that due to the double layer capacitance.

A starting point for the analysis of the cell constant for a planar cell will be the consideration of the effect of changes in the geometrical parameters d, h and w. Fig. 4 shows a schematic diagram of the nine cases generated by changing the magnitudes of w and h relative to d and a path through the five cases (arrowed) considered most relevant to the current study. Other areas of the diagram will be explored in a further study.

Case SE is essentially a one-dimensional case, where the interfacial capacitances are effectively in series with the resistance R_w of the electrolyte between the electrodes. The real part Z' of the impedance must therefore be nearly equal to R_w at all frequencies. Since the resistance R_d due to the electrolyte above each electrode is insignificant, the interfacial impedance will be dominated by the capacitance C_{dl} of the electrode | electrolyte interface. This case is therefore represented by the equivalent circuit of Fig. 2 with a resistance R_w and two capacitances C_{dl}, but without the effect of the permittivity capacitance C_g.

Case S was encountered briefly in our previous work [6], where a Warburg impedance effect was observed as a 45° line in the Nyquist plot following the high frequency intercept at R_w. This behaviour was explained according to a transmission line analogy, where R_d generated a Warburg impedance effect from the high frequency limit up to a frequency of $1/(R_d C_{dl})$ at which point the slope increased gradually to 90°, corresponding to a series combination of the interfacial capacitance and an electrolyte resistance due to a combination of both R_w and R_d. The transition from case S to case SW should correspond to an increase in the ratio of the width of the Warburg impedance region to the high frequency intercept.

Case W, obtained by increasing the height of the electrolyte, was not encountered in our previous work [6] and the form of the impedance was difficult to predict before the present simulations.

Case N is similar to that of two parallel microband electrodes [7] placed in an electrolyte solution of large height compared to the electrode width and separation. Here we may expect to observe that the cell constant is almost independent of the electrolyte height. In this case, the cell constant may be determined experimentally by immersing the cell in a solution of known conductivity and measuring the resistance.

Finally, an understanding of case O was one of the major goals of this work, namely to discover a method of determining the electrolyte height from the cell constants of a cell in which the parameters d, h and w are of the same order of magnitude.

3. Method of simulation

The spatial distribution of potential, ϕ, in the bulk conductor obeys Laplace's equation Eq. (3):

$$\nabla^2 \phi = 0 \tag{3}$$

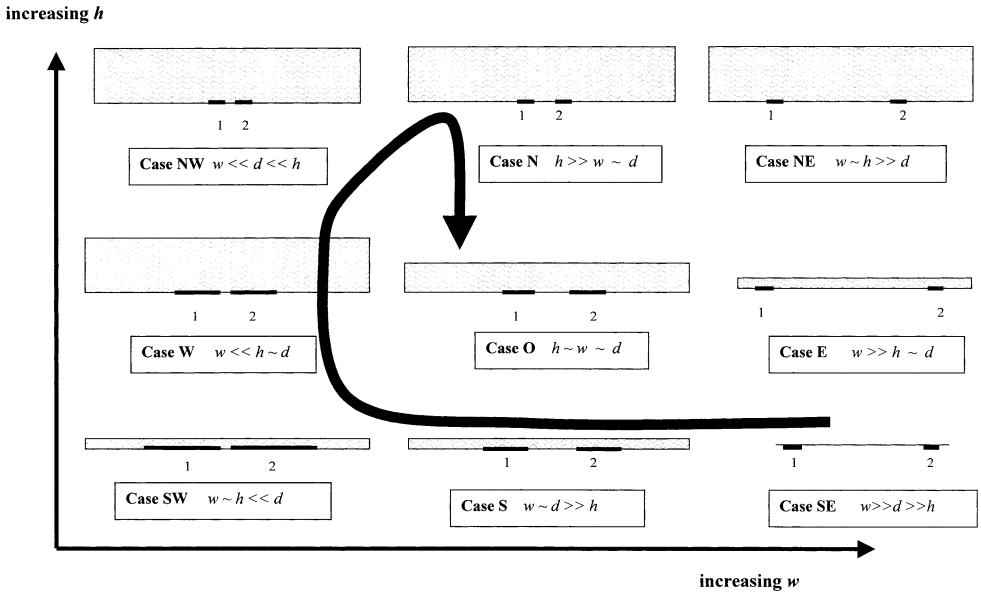

Fig. 4. The nine cases under consideration, distinguished by their aspect ratios, and the path taken in the course of the present analysis (arrowed).

Referring to the diagram of Fig. 3, we may assume that the current flux is zero at all boundaries of the sample except for the electrodes. At insulating boundaries the boundary condition is therefore

$$\underline{\hat{n}}\cdot\nabla\phi = 0 \tag{4}$$

where $\underline{\hat{n}}$ is the unit outward-pointing normal to the polymer.

Each electrolyte | electrode interface will be modelled as a simple capacitor representing ion blocking behaviour, although the theory could easily be extended to encompass more complicated interfacial effects. The boundary conditions at the electrodes 1 and 2 (see Fig. 3) are thus

$$\bar{C}\frac{\partial(\phi - \phi_1)}{\partial t} = \bar{\sigma}\underline{\hat{n}}_1\cdot\nabla\phi$$

$$\bar{C}\frac{\partial(\phi - \phi_2)}{\partial t} = \bar{\sigma}\underline{\hat{n}}_2\cdot\nabla\phi \tag{5}$$

where $\underline{\hat{n}}_1$ and $\underline{\hat{n}}_2$ are the unit outward normals to electrodes 1 and 2, respectively, $\bar{C}$ (F m^{-1}) is the capacitance per unit length of interface, ϕ (V) is the potential on the electrolyte side of the interface, and ϕ_1 and ϕ_2 are the excitation potentials on each electrode, which will be written

$$\phi_k = a_k\ \exp(\mathrm{i}\omega t) \tag{6}$$

Here ω is the angular frequency $2\pi f$ (radian s^{-1}) and the (real) a_k $(k = 1, 2)$ are the amplitudes of the potentials at each electrode. Note that for all the simulations described below we took $a_1 = 1$ and $a_2 = 0$ V.The potential at any point $\underline{x}$ within the polymer may be expressed as

$$\phi = \Phi(\underline{x})\exp(\mathrm{i}\omega t) \tag{7}$$

where the real and imaginary parts of $\Phi(\underline{x})$ are written

$$\Phi(\underline{x}) = \Phi'(\underline{x}) + \mathrm{i}\Phi''(\underline{x}) \tag{8}$$

Equating real and imaginary parts, the problem becomes

$$\nabla^2\Phi' = \nabla^2\Phi'' = 0 \tag{9}$$

in the polymer with boundary conditions

$$\underline{\hat{n}}\cdot\nabla\Phi' = \underline{\hat{n}}\cdot\nabla\Phi'' = 0 \tag{10}$$

at the insulating boundaries, and

$$-\omega\bar{C}\Phi'' = \bar{\sigma}\underline{\hat{n}}_k\cdot\nabla\Phi'$$

$$\omega\bar{C}(\Phi' - a_k) = \bar{\sigma}\underline{\hat{n}}_k\cdot\nabla\Phi'' \tag{11}$$

at the electrode interfaces $(k = 1, 2)$.

The simulations described in the current study were carried out using the finite element partial differential equation solver FASTFLOv3.0 [8]. The coupled Laplace equations were discretised in the standard way, and a simple Crout LU-decomposition was used to solve the resulting linear simultaneous equations. All calculations were carried out using a mesh consisting of 800 six-noded triangles; where appropriate, the mesh was concentrated at the edges of the electrodes adjacent to the inter-electrode gap as shown in Fig. 5. This proved to be particularly important in cases where the electrode gap width w was small compared to the electrode length d. The computational region for all calculations included 'end gaps' of width 200 μm to the left and right of electrodes 1 and 2, respectively. It may easily be confirmed that the dimensions of the end gaps have a negligible influence upon the results. Including pre- and

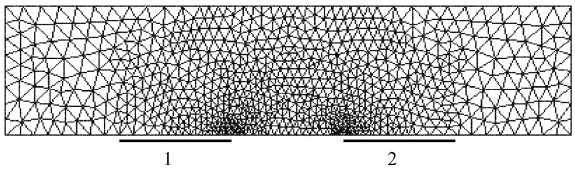

Fig. 5. Typical finite element mesh for simulations (in this case $d = h = w = 200$ μm).

post-processing, each of the calculations ran in a few seconds of CPU time on a standard 600 MHz desktop machine running under LINUX. The usual convergence tests were carried out to establish that the numerical results were insensitive to further mesh refinement: in all cases further doubling the number of mesh elements to 1600 made a difference of less than 1% to the results.

The primary output of the numerical simulations is the real and imaginary parts of the cell current per unit electrode breadth, I/b (A m^{-1}). Table 1 shows an example output for case N in which the sample height, $h = 1000$ μm is five times as large as both the gap width, w and the electrode length, d. Comparing the calculated currents on each electrode provided an extra numerical check on the results; despite inaccuracies due to the finite mesh size, the observed 1% variation showed that the numerical errors were small. At very high frequency the imaginary current changes sign; this is also because of small numerical errors. The absolute currents at each electrode were averaged to obtain the real and imaginary parts I' and I'' of the cell current as functions of frequency.

The impedance per unit reciprocal length is given by Eq. (12)

$$Zb\ (\Omega\ \mathrm{m}) = V/(I/b) \tag{12}$$

where $V = 1$ V.

The product of the complex cell constant K and the electrode breadth, b, (displayed in the last two columns of Table 1) may then be calculated by taking the reciprocal of the current and multiplying by the conductivity as shown in Eq. (13).

$$\bar{K} = \bar{K}' + \mathrm{i}\bar{K}'' = Kb = \sigma Zb = \sigma V(I/b)^{-1}\ \text{(dimensionless)} \tag{13}$$

The limiting values of the real parts of $\bar{K}$ at high and low frequency were noted in each case, and hereafter will be designated by $\bar{k}_\infty$ and $\bar{k}_0$, respectively (dimensionless).

Table 1
Raw results produced by the simulation

Electrode width	$d = 2 \times 10^{-4}$ m
Electrode gap	$w = 2 \times 10^{-4}$ m
End gaps	$= 2 \times 10^{-4}$ m
Polymer height	$h = 1 \times 10^{-3}$ m
Aspect ratio	$= 1$
Conductivity	$\sigma = 1$ S m^{-1}
Capacitance per unit area	$C = 0.1$ F m^{-2}

Frequency ω/rad s^{-1}	Real current/A m^{-1}	Im current/A m^{-1}	Real current/A m^{-1}	Im current/A m^{-1}	Dimensionless complex cell constant	
	Electrode 1	Electrode 1	Electrode 2	Electrode 2	K'	K''
1000	−1.42003E−04	9.53066E−03	1.41291E−04	−9.48943E−03	1.565835	105
2500	−8.86468E−04	2.37987E−02	8.82025E−04	−2.36958E−02	1.565831	42
5000	−3.53093E−03	4.73989E−02	3.51324E−03	−4.71941E−02	1.565814	21
10 000	−1.38896E−02	9.32427E−02	1.38201E−02	−9.28411E−02	1.565741	11
20 000	−5.21055E−02	1.75014E−01	5.18455E−02	−1.74271E−01	1.565458	5
25 000	−7.77905E−02	2.09135E−01	7.74034E−02	−2.08256E−01	1.56524	4
30 000	−1.06241E−01	2.38163E−01	1.05714E−01	−2.37174E−01	1.564993	4
40 000	−1.66970E−01	2.81154E−01	1.66148E−01	−2.80024E−01	1.564344	3
50 000	−2.27082E−01	3.06477E−01	2.25975E−01	−3.05295E−01	1.563544	2
60 000	−2.82352E−01	3.18261E−01	2.80991E−01	−3.17095E−01	1.562601	2
70 000	−3.31003E−01	3.20593E−01	3.29429E−01	−3.19488E−01	1.561537	2
80 000	−3.72787E−01	3.16783E−01	3.71041E−01	−3.15767E−01	1.56037	1
90 000	−4.08228E−01	3.09239E−01	4.06347E−01	−3.08326E−01	1.559116	1
100 000	−4.38143E−01	2.99600E−01	4.36161E−01	−2.98796E−01	1.5578	1
200 000	−5.77248E−01	2.02921E−01	5.75143E−01	−2.02917E−01	1.544026	1
500 000	−6.45490E−01	8.89404E−02	6.43894E−01	−8.90489E−02	1.522123	0
100 000	−6.56989E−01	3.06925E−02	6.55119E−01	−3.07426E−02	1.52093	0
2 000 000	−6.46088E−01	−1.01429E−02	6.44225E−01	9.35980E−03	1.549657	0
5 000 000	−6.11239E−01	−2.63832E−02	6.10572E−01	2.54201E−02	1.633977	0
10 000 000	−5.95622E−01	−1.17965E−02	5.95314E−01	1.74487E−02	1.678339	0

In order to express the cell constants in the normal three-dimensional units we finally divided the $\bar{K}$ values by a b value of 0.5 mm which corresponds to the dimensions of our prototype cell. $\bar{k}_\infty$ should be thought of as the real cell constant at high frequency, where the interfacial impedance disappears. $\bar{k}_o$, on the other hand, is a real value obtained by extrapolating the complex impedance at low frequency to the real axis. In previous methods (using, for example, electrode immersion for liquids or cylindrical cells for polymers) of determining electrolyte conductivity it has been necessary to consider only a single real cell constant k. This is because in those cases, the values k were identical to both k_∞ and k_o. In this work, however, it will transpire that this is no longer true, and that a consideration of the differences between k_∞ and k_o will give valuable information about both the conductivity and the thickness of the polymer in a planar cell.

4. Results and discussion

We now turn to a detailed discussion of the results for each of the cases highlighted above except for case SE which, as noted above, reduces to a one-dimensional model.

The simulation results of Fig. 6 cover cases S ($d = 200$ μm, $h = 20$ μm, $w = 200$ μm) and SW ($d = 200$ μm, $h = w = 20$ μm) along with the transition from S to SW. We observe a separation of the cell constant plots into two regimes—a Warburg impedance at high frequency and a vertical spur at low frequency. The real parameters, $\bar{k}_\infty$ and $\bar{k}_o$ may be determined at high and low frequency limits by extrapolation of the 45° line and spur, respectively to the real axis. Fig. 7 shows the dependence of the two cell constants on w/h when $h = 20$ μm. We find that the high frequency constant $\bar{k}_\infty$ fits very well to a linear function of w/h,

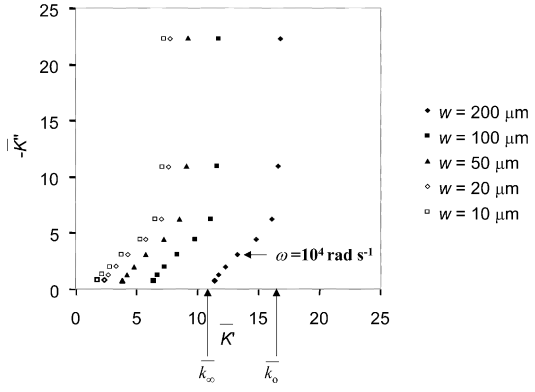

Fig. 6. Nyquist plot of complex cell constants from finite element simulation results for cases S, SW and the transition between them ($h = 20$ μm, $d = 200$ μm). Points are shown at three points per decade from the maximum frequency of 10^5 rad s^{-1}.

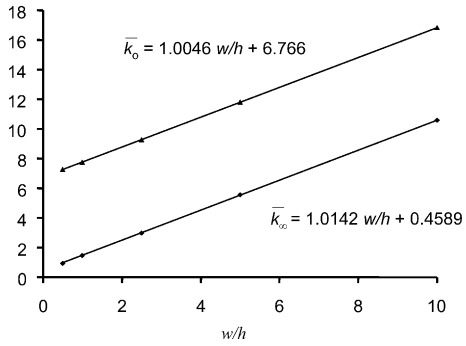

Fig. 7. Dependence of the cell constants calculated by finite element simulation (symbols) on w/h ($h = 20$ μm, $d = 200$ μm). The two solid lines are the best-fit straight lines through the data.

$$\bar{k}_\infty = \alpha w/h + \beta, \quad \text{where } \alpha = 1.014 \text{ and } \beta = 0.459 \tag{14}$$

The fact that the value of α is extremely close to unity is consistent with the obvious one-dimensional analysis where it is assumed that the current density is constant.

Over most of the range considered $\alpha w/h \gg \beta$ and therefore a good approximation to $\bar{k}_\infty$ for both the cases S and SW is

$$\bar{k}_\infty \approx w/h \tag{15}$$

The low frequency constant, $\bar{k}_o$, is larger than $\bar{k}_\infty$ by an almost constant value. The difference $(\bar{k}_o - \bar{k}_\infty)$ has a value of about 6.7. This can be explained according to the transmission line model shown in Fig. 8, which accounts for the distribution of the double layer capacitance over an increasing resistance path toward the outer edge of the electrode. The standard transmission line formula for impedance [9] and its low frequency approximation are given in Eq. (16).

$$Z = (R_d/G_{dl})^{1/2} \coth[(R_d G_{dl})^{1/2}] \sim 1/G_{dl} + R_d/3 \quad \text{for } \omega \ll (R_d C_{dl})^{-1} \tag{16}$$

where R_d denotes the distributed electrolyte resistance (as shown in Fig. 8) and G_{dl} ($= i\omega C_{dl}$) the interfacial admittance.

In the present case, $d/h = 10$ and $R_d = d/(h\bar{\sigma})$ because of the one-dimensional nature of the distributed resistance. Therefore the total effective resistance, Z_{eff} for the electrolyte paths above both electrode interfaces (added in series) is, to leading order in $\omega R_d C_d$,

$$Z_{eff} = 2R_d/3 = (2/3)(d/h\bar{\sigma}) \tag{17}$$

and thus

$$(\bar{k}_o - \bar{k}_\infty) = \bar{\sigma} Z_{eff} = 2/3(d/h) \approx 6.7 \tag{18}$$

This provides a satisfactory explanation of the value of the difference between the two cell constants noted above and also provides a useful quantitative expression for the determination of the conductivity from experimental impedance results in cases where $h/d \ll 1$ and the electrolyte height is known accurately.

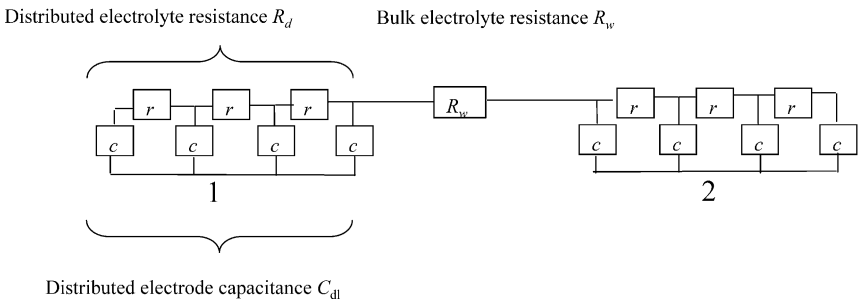

Fig. 8. A transmission line model for explaining planar electrode behaviour in cases S, SW, S→SW. (The individual components r and c represent the resistance and capacitance per unit electrode length of the distributed parameter network.)

The simulation results shown in Fig. 9 illustrate how the current paths depend on frequency in cases S, SW and S→SW. At the highest frequency the current paths lie mainly between the closest points on the electrodes. At intermediate frequencies corresponding to the Warburg impedance the current spreads outwards until, at the lowest frequency, the whole of the electrode is involved.

The frequency dependence of the real part of the Warburg impedance is shown in the plot of $\bar{K}'$ versus $\omega^{-1/2}$ in Fig. 10. This corresponds to the high frequency approximation of Eq. (16), which gives

$$Z \sim (R_d/G_{dl})^{1/2} \sim (1-i)(2\omega)^{-1/2}(R_d/C_{dl})^{1/2}$$

$$\text{for } \omega \gg (R_d C_{dl})^{-1} \tag{19}$$

The inclined line of the plot corresponds to the transition between $\bar{k}_0$ and $\bar{k}_\infty$ according to Eq. (19), and confirms that the frequency dependence is as expected for the equivalent transmission line circuit.

This terminates our analysis of cases S, SW, and the transition between them. We conclude that the behaviour of planar cells with very thin electrolyte layers may be explained using the notion of a complex cell constant. The theory shows that the conductivity may be obtained by measuring either the high frequency limiting value or the real intercept at low frequency of the impedance, and using Eqs. (19) and (16), respectively. We note,

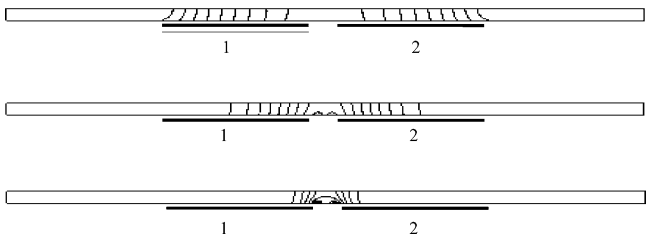

Fig. 9. Contours of current distribution from finite element simulations at low, medium and high frequencies. Contours of the quantity $(\underline{E}\cdot\underline{E})^{1/2}$ are shown in 10% increments from 0.1 $\max(\underline{E}\cdot\underline{E})^{1/2}$ to 0.9 $\max(\underline{E}\cdot\underline{E})^{1/2}$ for the case $w = 20$ μm, $h = 20$ μm, $d = 200$ μm, $\bar{\sigma} = 0.1$ S, $\bar{C} = 0.1$ F m^{-1} for frequencies $\omega = 1000$ rad s^{-1} (top picture), $\omega = 10\,000$ rad s^{-1} (middle picture) and $\omega = 100\,000$ rad s^{-1} (bottom picture).

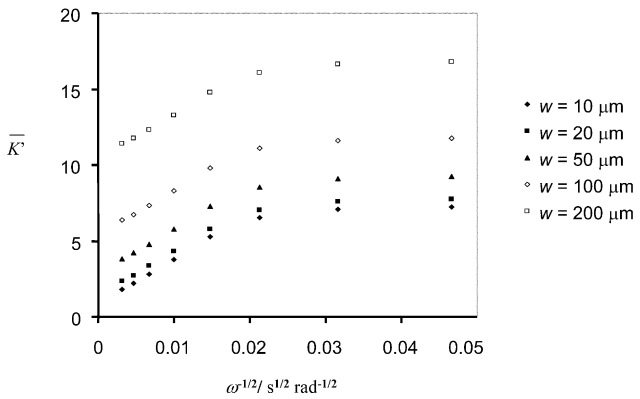

Fig. 10. Plot of the real part $\bar{K}'$ of the cell constant vs. (frequency)$^{-1/2}$ showing finite transmission line behaviour.

however, that the application of these equations requires accurate knowledge of the sample height h.

We now investigate the transition from case SW to case W ($w \ll h \sim d$). The complex cell constant is shown in the Nyquist plot of Fig. 11, where the gap width is held constant while the sample height is increased. We observe that the 45° (Warburg) line that was present in the previous cases discussed has now been replaced by a line with greater slope. This may be interpreted as a

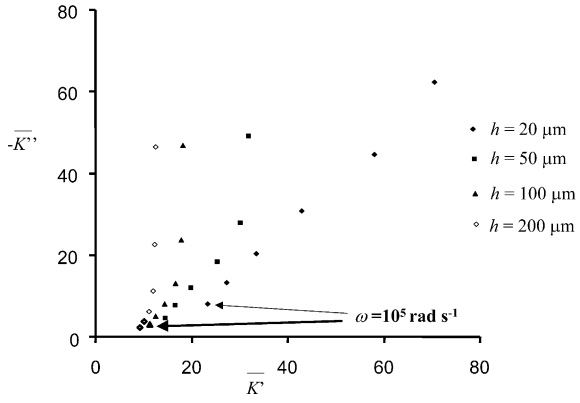

Fig. 11. Nyquist plot of complex cell constants from finite element simulation results for cases SW, W and the transition between them ($w = 20$ μm, $d = 200$ μm). Points are shown at three points per decade from the maximum frequency of 10^5 rad s^{-1}.

constant phase element (CPE). CPE behaviour is a common subject of debate in impedance analysis, where its origins have been attributed to various phenomena such as electrode roughness or non-ideal capacitive behaviour. We shall see that a CPE can arise (albeit over a restricted frequency range) purely from a simple geometrical effect. This is an important finding that will be discussed further below.

Case N ($h \gg w \sim d$) corresponds to a pair of micro-band electrodes. The complex cell constant $\bar{K}$ is shown in the Nyquist plot of Fig. 12. We observe that the real part is almost constant, i.e. $\bar{k}_o \sim \bar{k}_\infty$ and that the magnitude of the imaginary part decreases with increasing frequency. This is suggestive of a series combination of a resistance (real part) and a capacitance (imaginary part). We further note from Fig. 12 that, as might be expected, for each frequency the imaginary part does not change significantly with w. However, the real part decreases monotonically, but not linearly, with w.

The change in the cell constant $\bar{k}_o$ with w is shown in Fig. 13. The results may be compared with the analytical (SC) solutions of Jacobs et al. [10], who give the formula:

$$\bar{k} = \frac{2\kappa(w/(w+2d))}{\kappa'(w/(w+2d))} \tag{20}$$

where $\kappa(m)$, the complete elliptical integral of the first kind, is given by

$$\kappa(m) = \int_0^1 \frac{\mathrm{d}t}{\sqrt{(1-t^2)(1-m^2t^2)}} \tag{21}$$

and $\kappa'(m) = \kappa(\sqrt{1-m^2})$.

Eq. (20) is strictly applicable only in cases where the electrolyte sample extends for an infinite distance both above and either side of the electrodes. Nevertheless, we note that the agreement between Eq. (20) and the simulation results shown in Fig. 13 is remarkably good, therefore further increasing our confidence in the reliability of the simulation method.

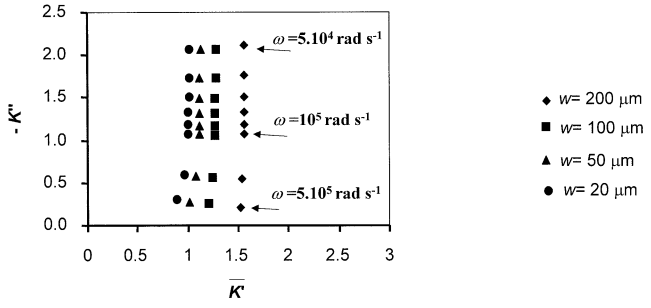

Fig. 12. Nyquist plot of complex cell constants from finite element simulation results for cases N, NW and the transition between them ($h = 1000$ μm, $d = 200$ μm).

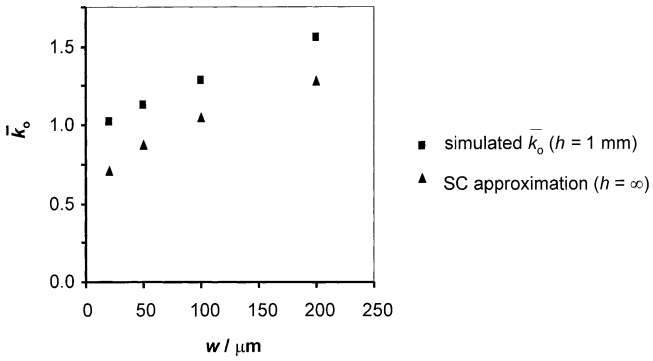

Fig. 13. Values of $\bar{k}_o$ from finite element simulation compared to SC calculations for case N ($h = 1000$ μm, $d = 200$ μm).

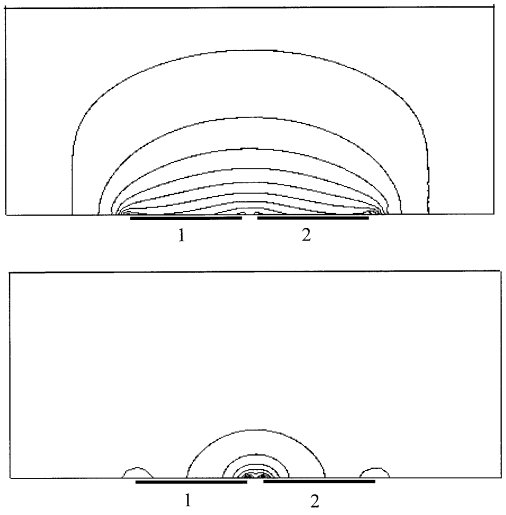

Fig. 14. Contours of current distribution from finite element simulations at low and high frequencies. Contours of the quantity $(\underline{E}\cdot\underline{E})^{1/2}$ are shown in 10% increments from 0.1 max $(\underline{E}\cdot\underline{E})^{1/2}$ to 0.9 max $(\underline{E}\cdot\underline{E})^{1/2}$ for the case $w = 20$ μm, $h = 1000$ μm, $d = 200$ μm, $\bar{\sigma} = 0.1$ S, $\bar{C} = 0.1$ F m^{-1} for frequencies $\omega = 1000$ rad s^{-1} (top picture) and $\omega = 100\,000$ rad s^{-1} (bottom picture).

Fig. 14 shows the location of the main current paths for a typical case where h is much greater than d and w. We note that the current paths do not extend far above the electrode at low frequency and are even more localised at high frequency. Evidently we may therefore expect the cell constants $\bar{k}_\infty$ and $\bar{k}_o$ to be relatively insensitive to the sample height, h. The similarity in the values of $\bar{k}_\infty$ and $\bar{k}_o$ (as observed in Fig. 12) is explained by the observation that, whatever the frequency, most of the potential drop is estimated to be in the region close to the electrode surface.

Although this case could be used as a basis for measuring polymer electrolyte conductivity it has the disadvantage of requiring very thick films, so that the object of minimising the sample quantity would be defeated. Therefore we shall continue to the final case O, where the electrode width, gap width, and electrolyte height are all similar to each other.

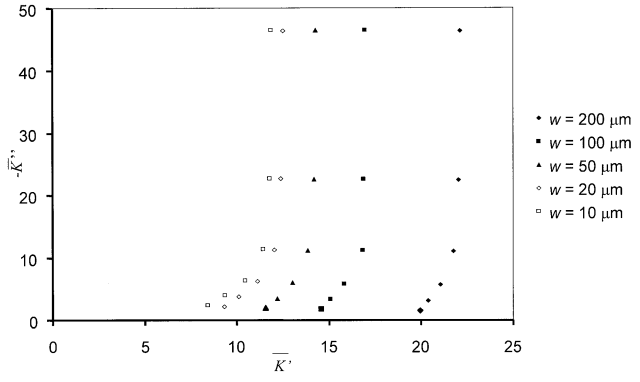

Fig. 15. Nyquist plot of complex cell constants from finite element simulation results for cases W, O and the transition between them h200 m, d200 m. Points are shown at three points per decade from the maximum frequency of 105 rad s1.

Simulation results for a range of cell geometries close to case O are displayed in the Nyquist plot of Fig. 15. In the investigation above of the transition between cases SW and W we noted the existence of CPE behaviour: the results of Fig. 15 also show linear regions with slopes greater than 45°. We also note that both $\bar{k}_o$ and $\bar{k}_\infty$ increase with increasing w/h.

On close examination it was found that the gradient, $-\mathrm{d}\bar{K}''/\mathrm{d}\bar{K}'$, of the Nyquist plot at high frequency was not quite constant. The gradient was therefore measured at the high frequency intercept as shown in Fig. 16, where the scale of the imaginary axis has been magnified to show that well-defined gradients and intercepts may be obtained. Fig. 17 further shows the dependence of the gradient $-\mathrm{d}\bar{K}''/\mathrm{d}\bar{K}'$ upon h/d for various values of w/d. We note that *the gradient is a sensitive indicator of the sample height*. The dependence of the gradient on the sample height may be further investigated; we observe from Fig. 17 that the data points for the case $w/d = 1$ fall almost on a straight line for the whole range of h/d between 0 and 1. For smaller values of w/d the data deviate from this line approximately when h/d exceeds w/d.

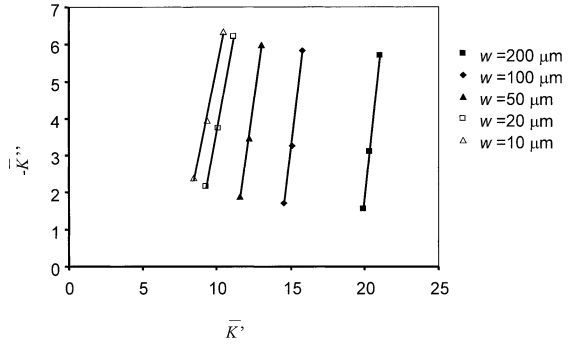

Fig. 16. Magnification of high frequency part of Nyquist plot in Fig. 15, showing finite element simulation results (symbols) and best-fit straight lines (solid lines) for cases W, O and the transition between them ($h = 200$ μm, $d = 200$ μm).

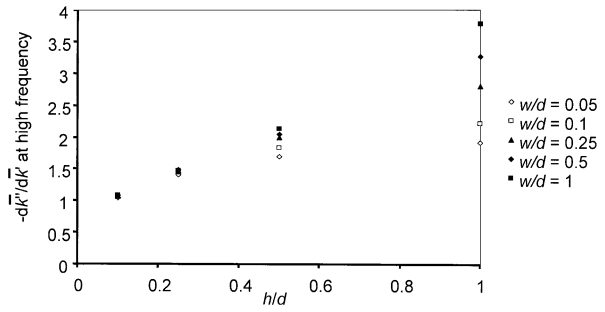

Fig. 17. Finite element simulation results for gradient $-\mathrm{d}\bar{K}''/\mathrm{d}\bar{K}'$ at high frequency as a function of h/d for various w/d ($d = 200$ μm).

These results fulfil the major objective of this study. They not only provide a method for determining the sample height but also indicate the optimum cell dimensions for measuring polymer film thicknesses within a given range. For example, given the range $h = 10$–100 μm commonly encountered for films formed by solvent casting, the cell should have both a gap width w and an electrode width d of approximately 100 μm for accurate determination of h by this method. In short, cells of type O are the most convenient if the polymer height is uncertain.

The above result will be useful only if the high frequency behaviour is not affected by parallel admittances (such as the input capacitance of the instrumentation or the dielectic permittivity of the sample itself). In practice, however, at high frequency limits the measured impedance is sometimes obscured by such effects. We shall therefore seek a further relationship between the complex cell constant and the geometry in case O.

The values of $\bar{k}_\infty$ and $\bar{k}_o$ and their dependence on w for given values of h are shown in Fig. 18. We should remember here that the measured quantity is Z, not k; however, *ratios between two k values can be obtained from experiment in the form of the ratio between two impedance values taken at different values of w*.

We observed above that for cases S and SW ($h/d \ll 1$) the simple relationship $\bar{k}_o - \bar{k}_\infty = 0.67\ d/h$ applies. The results of Fig. 19 (which include a point for $d = 300$ μm to emphasise the dependence on d), indicate that the same relationship applies for h/d values approaching 1. The fact that Eq. (17) still applies in case O is a surprisingly simple result, which, as yet, appears to have no theoretical explanation. This result unfortunately does not give a method for determining h, however, since the ratio of two values of $\bar{k}_o - \bar{k}_\infty$ is insensitive to h.

Fig. 20 shows the individual values of $\bar{k}_\infty$ and $\bar{k}_o$, normalised with respect to their values at $w = 200$ μm by calculating the ratios $\bar{k}_\infty/\bar{k}_{\infty,200}$, etc. The upper plots show the normalised values plotted for various h as a function of w. The lower plots show the same quantities plotted as functions of h for various w. We notice that,

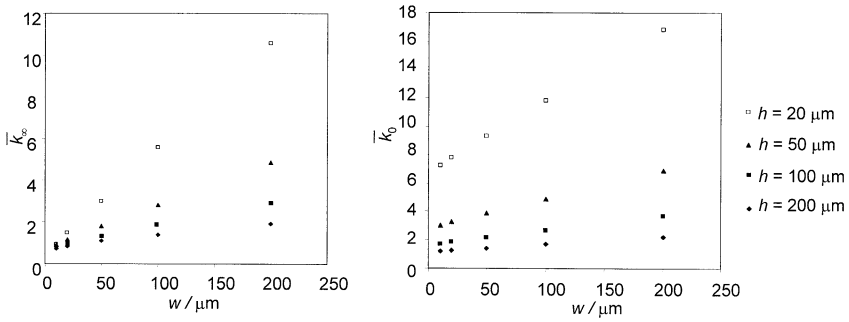

Fig. 18. Dependence of $\bar{k}_\infty$ and $\bar{k}_o$ on w from finite element simulation results for various values of h ($d = 200$ μm).

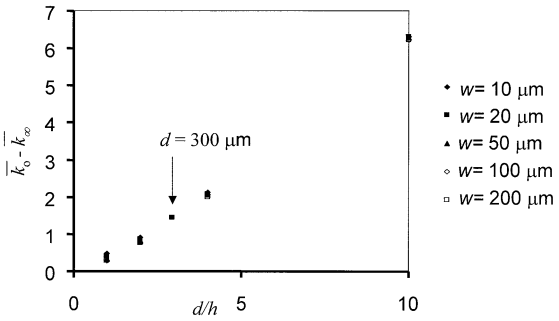

Fig. 19. Finite element simulation results showing the dependence of the quantity $\bar{k}_o - \bar{k}_\infty$ on d/h for various w ($d = 200$ μm). (Note: a point for $d = 300$ μm has been included to emphasise the dependence on the quantity h/d rather than simply h.)

though the dependence of $\bar{k}_o/\bar{k}_{o,200}$, on h is rather weak, $\bar{k}_\infty/\bar{k}_{\infty,200}$ displays a stronger dependence on h, which may be exploited in two ways. First, the lower plot could be used to obtain the value of h for a given w from $\bar{k}_\infty/\bar{k}_{\infty,200}$. Perhaps a more robust method, however, is to measure $\bar{k}_\infty/\bar{k}_{\infty,200}$ for a range of different values of w and then match the experimental curve against the appropriate simulation curve in the upper right hand plot of Fig. 20. Using this latter method, a good fit would confirm that the theory and experiment are consistent.

The method suggested above depends on obtaining an accurate value of $\bar{k}_\infty$ by extrapolation of the results to the high frequency limit. Again we must be aware that dielectric, or stray capacitances may be problematic, although not so severely as in the method that uses the high frequency limit of the gradient. To eliminate the high frequency problem altogether, it would be necessary to use the values of $\bar{k}_o/\bar{k}_{o,200}$ which, as mentioned above, display a weak dependence on h. Alternatively, we could investigate case E, where it might be expected that $\bar{k}_o/\bar{k}_{o,200}$ would approach $\bar{k}_\infty/\bar{k}_{\infty,200}$. This approach may be the subject of further simulation work (if appropriate) after an experimental evaluation of cases S to O.

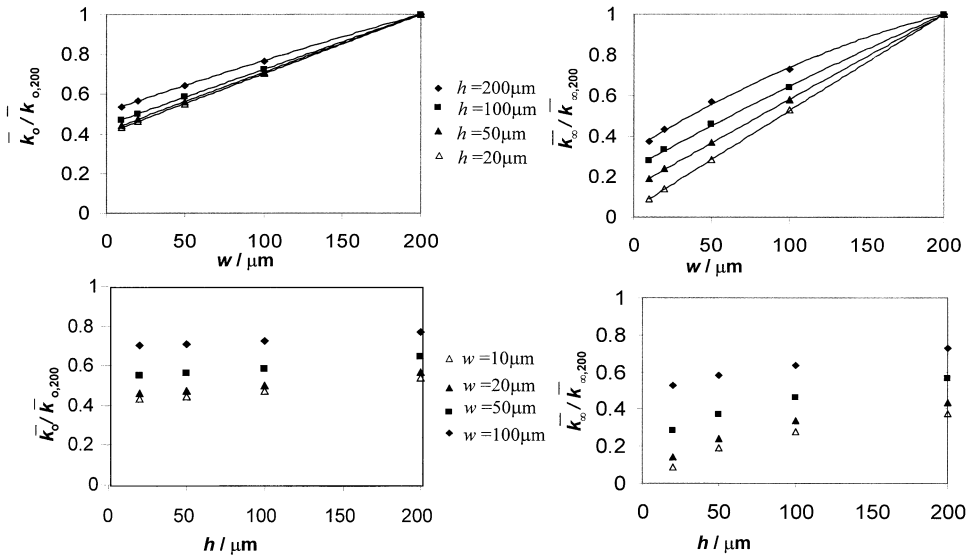

Fig. 20. Finite element simulation results for normalised $\bar{k}_\infty$ and $\bar{k}_o$ as a function of h for various values of w (lower plots), ($d = 200$ μm). The upper plots show the same quantities as a function of w for various values of h ($d = 200$ μm) together with fitted calibration curves for experimental determination of h.

5. Conclusions

The finite element simulation technique has been applied to the calculation of the complex impedances of planar cells for a wide range of cell geometries. For all cell geometries where suitable theoretical models exist, the finite element calculations gave consistent results. For many cell geometries of practical interest no suitable theoretical models exist, and it is in these cases that the finite element method has proved to be particularly valuable.

Our analysis has further shown that, as far as planar electrode cells are concerned, the notion of a complex cell constant is a particularly useful one as it allows the impedance of the cell to be described in a fashion that is independent of the conductivity. In all the cases examined, the Nyquist plot of the complex cell constant may be conveniently characterised by the high and low frequency limits k_∞ and k_o of the real part of the cell constant, and the gradient of the line which joins the high frequency intercept and the transition between high and low frequency behaviour.

The values of k_∞ and the gradient were both found to be particularly sensitive to the cell height, i.e. the polymer film thickness. Consequently, cell designs where it is possible to measure both the height of the polymer region and the polymer conductivity by carrying out suitably designed experiments have been highlighted. In these cases, the optimal measurement parameters have also been identified.

Acknowledgements

The authors wish to thank Professor Phil Bartlett (University of Southampton) for suggesting the use of the gap electrode for polymer electrolyte measurement and Professor Julian Gardener (University of Warwick) for useful discussions.

References

[1] J.M. Tarascon, M. Armand, Nature, 414 (2001) 359.
[2] A. Schechter, R.F. Savinell, Solid State Ionics 147 (2002) 181.
[3] P.M.S. Monk, R.J. Mortimer, D.R. Rosseinsky, Electrochromism, VCH, Weinheim, 1995, p. 44.
[4] J.R. Owen, E. Linden, Br. Polymer J. 20 (1988) 237.
[5] P.G. Bruce, in: J.R. MacCallum, C.A. Vincent (Eds.), Polymer Electrolyte Reviews, vol. 1, Elsevier Applied Science, London, 1987, pp. 250–254.
[6] I.M. Ismail, J.R. Owen, Solid State Ionics 85 (1996) 163.
[7] C. Amatore, B. Fosset, Anal. Chem. 68 (1996) 4377.
[8] NAG Ltd. FASTFLO User Manual. Oxford, England: Numerical Algorithms Group (2001).
[9] J.R. Macdonald (Ed.), Impedance Spectroscopy, Wiley-Interscience, New York, 1987, p. 95.
[10] P. Jacobs, A. Varlan, W. Sansen, J. Med. Bio. Eng. Comp. 33 (1995) 802.